PHYSICAL REVIEW B **110**, 075420 (2024)

Synthetic Weyl points in plasmonic chain with simultaneous inversion and reflection symmetry breaking

Huizhou Wu,[1] Z. Z. Liu,[1,2] and Jun-Jun Xiao[1,3,*]

[1]College of Electronic and Information Engineering and Shenzhen Engineering Laboratory of Aerospace Detection and Imaging, Harbin Institute of Technology (Shenzhen), Shenzhen 518055, China

[2]Research Center for Advanced Optics and Photoelectronics, Department of Physics, College of Science, Shantou University, Shantou 515063, China

[3]College of Integrated Circuit, Harbin Institute of Technology (Shenzhen), Shenzhen 518055, China

(Received 8 May 2024; revised 29 June 2024; accepted 7 August 2024; published 15 August 2024)

Photonic nanoparticle arrays present a unique platform for exploring optical topological phenomena. In this study, we incorporate the concept of synthetic dimensions into the plasmonic system, which allows us to investigate Weyl physics within a chain of metallic nanoparticles. By introducing two extra periodic positional parameters into the chain, we construct a synthetic three-dimensional space that gives rise to synthetic Weyl points (WPs). Our findings reveal that the chain maintains topologically protected edge modes even when the inversion symmetry of the chain is broken. The topological properties of these edge modes are intrinsically linked to the WPs within the synthetic three-dimensional space. However, degenerate edge modes emerge exclusively in chains possessing inversion symmetry. Furthermore, we uncover the bulk-edge correspondence in the chains, yielding a deeper understanding of the topological nature of edge modes in systems without symmetry. Our research not only clarifies the topological origin of a class of edge states within asymmetric nanoparticle chains but also provides perspectives for realizing higher-dimensional topological effects in nanoparticle arrays.

DOI: 10.1103/PhysRevB.110.075420

I. INTRODUCTION

Over the past decade, topological electronic materials and topological classical wave systems have attracted considerable attention due to their ability to support localized edge modes that are resilient to backscattering from disorder and impurities [1–19]. The phenomenon of topological protection, which leads to these edge modes, is generally associated with the inherent symmetries of the materials [3–9]. For instance, in one-dimensional (1D) Hermitian systems, the presence of inversion symmetry guarantees the existence of a quantized Zak phase [6–9], which plays an important role in the prediction and characterization of edge modes through the established principle of bulk-edge correspondence [8–10]. Extending beyond the realm of symmetry-protected edge modes, topological edge states have been identified in numerous systems that do not conform to a conventional quantized topological index, such as n-root topological insulators [11–16] and 1D trimer lattices with broken inversion symmetry [17,18,20]. In the former case, the topological nature of n-root topological insulators is derived from the squared parent Hamiltonian [11,14], while the latter's topology emerges from the associated two-dimensional (2D) parent system [17].

In recent years, the concept of synthetic dimension has been extensively employed to realize higher-dimensional topology in low-dimensional structures [21–31], offering a new perspective for understanding the origins of topology in asymmetric systems. In particular, Weyl physics has been investigated in 1D and 2D symmetry-broken structures using synthetic dimensions, where the emergence of edge states is attributed to the topology of synthetic Weyl points (WPs) [25–29]. A WP is a nodal degenerate point in a three-dimensional (3D) reciprocal space, characterized by linear dispersion in all directions near it [32–37]. Each WP is identifiable as a monopole, i.e., a source or sink of Berry flux in the reciprocal space or synthetic parameter space, and possesses a nonzero topological charge [32,38]. The WP can be annihilated only by merging two WPs with opposite topological charges [32,36]. As a result, WPs are protected by the underlying topology and are stable against small perturbations [36,39]. Numerous fascinating phenomena associated with topologically protected WPs have been theoretically predicted and experimentally observed in both real and synthetic 3D systems [25–29,40–42], including Fermi arc surface states and chiral anomalies.

In this study, we explore synthetic Weyl physics within a particular kind of metal nanoparticle chain. Light-excited metal nanoparticles couple with neighboring particles due to localized surface plasmons [43–47]. The electromagnetic coupling between metal nanoparticles can be modulated by their spatial distance [45,47]. By appropriately contracting or expanding the unit cells, various topological phases can be achieved in the plasmonic system, providing an ideal platform for exploring topological effects at the nanoscale [47–54]. Incorporating synthetic dimensions into the plasmonic system further enriches the ways to explore their topological

---

[*] Contact author: eiexiao@hit.edu.cn

properties and opens new avenues for the engineering of low-dimensional nanoscale topological states.

To study synthetic Weyl physics in the nanoparticle chain, we utilize the positional parameters of nanoparticles as an additional degree of freedom to create a synthetic dimension. Unlike layered crystals [25,26,30], the synthetic positional parameter dimensions are periodic and closed, allowing synthetic WPs with opposite topological charge to coexist in the parameter space of the chain, mimicking real 3D Weyl systems [40–42,55–57]. This setup facilitates the investigation of the bulk-edge correspondence in synthetic Weyl systems, which is currently underexplored. Furthermore, the chain exhibits either inversion symmetry or broken symmetry as the positional parameters vary. The bulk-edge correspondence associated with synthetic WPs ensures the existence of edge states in both inversion-symmetric and inversion-symmetry-broken chains, enabling us to explore the relationships between edge states in these scenarios. The results are examined using the coupled dipole approximation method (CDM) [46,54] and verified through full-wave simulations with a commercial solver (COMSOL MULTIPHYSICS) of the finite-element method (FEM).

II. SYNTHETIC WEYL POINTS IN THE PLASMONIC CHAIN

The plasmonic chain under consideration comprises four silver ellipsoidal nanoparticles (ENPs) within each unit cell. The permittivity of silver is characterized by the Drude model. The ENPs have a major axis length of 20 nm and a minor axis length of 10 nm. We focus solely on the major axis dipole resonance mode (near $f = 690\,\text{THz}$), as the minor axis dipole resonance (near $f = 850\,\text{THz}$) is sufficiently separated in the frequency domain from the former [51,54]. More details regarding the optical response of such individual ENPs are provided in Appendix A. Figure 1(a) illustrates the relative positions of the four ENPs, labeled A, B, C, and D within a unit cell. The major axes of the ENPs are arranged in the xy plane and aligned at the same 45° angle with respect to the positive x axis. The horizontal distances between the centers are maintained as

$$\begin{aligned} x_{\text{AB}} &= d_0 + \Delta x, \\ x_{\text{BC}} &= d_0 - \Delta x, \\ x_{\text{CD}} &= d_0 + \Delta x, \end{aligned} \tag{1}$$

where $\Delta x = 3$ nm, $d_0 = d/4$, and $d = 160$ nm is the unit-cell length. It can be inferred that the intercellular distance equals x_{BC}. The vertical positions of the ENPs are given by

$$\begin{aligned} y_{\text{A}} &= h\cos(p\pi), y_{\text{C}} = -h\cos(p\pi), \\ y_{\text{B}} &= h\cos(q\pi), y_{\text{D}} = -h\cos(q\pi), \end{aligned} \tag{2}$$

where $h = 5$ nm and p and q are the periodic parameters, which naturally play the role of the synthetic dimensions. The parameters p and q, in conjunction with the Bloch wave vector k_x of the chain, construct a synthetic 3D space, providing an appropriate platform for investigating Weyl physics in the plasmonic system. An alternative strategy that warrants consideration involves oscillating the ENPs in the horizontal direction; however, our computational analyses indicate that the range of coupling variation between ENPs in such a scenario is remarkably narrower. More comprehensive comparisons are provided in Appendix B.

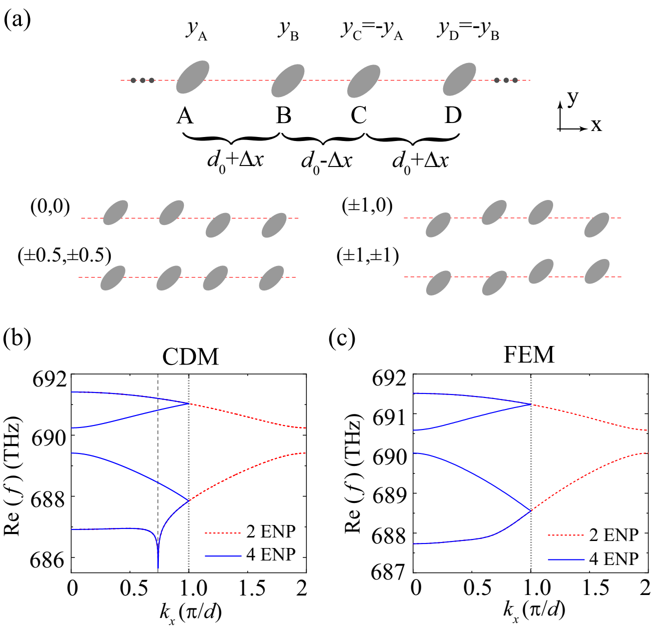

FIG. 1. (a) Top: Schematic of the ENP chain with $d_0 = 40$ nm and $\Delta x = 3$ nm. Bottom: ENP chain with different (p, q). (b) and (c) Plasmonic band structures calculated by CDM and FEM, respectively, with $(p, q) = (\pm 0.5, \pm 0.5)$.

Within the dipole approximation, the optical responses of such a chain can be described by the CDM equations [43,45–47,54],

$$\frac{1}{\alpha(\omega)} p_n = E_0(\mathbf{r}_n) + \frac{\omega^2}{c^2} \sum_{m \neq n} M(\mathbf{r}_n - \mathbf{r}_m, \omega) p_m, \tag{3}$$

where $p_{n,m}$ and $\mathbf{r}_{n,m}$ represent the dipole moments and positions of the (n, m)th ENP in the chain, respectively. In Eq. (3) α, ω, c, and E_0 are the polarizability of the ENP (see Appendix A), the angular frequency, the speed of light in free space, and the external incident field, respectively. Here M describes the interaction between the nth and mth ENPs and is given by

$$M(\mathbf{r}_n - \mathbf{r}_m, \omega) = [\overleftrightarrow{\mathbf{G}}(\mathbf{r}_n - \mathbf{r}_m, \omega) \cdot \mathbf{I}_m]^T \cdot \mathbf{I}_n, \tag{4}$$

where $\mathbf{I}_{n,m}$ represents the unit vector in the direction of the major axis of the ENP and T denotes the transpose operation. The free space dyadic Green's function $\overleftrightarrow{\mathbf{G}}$ reads

$$\begin{aligned} \overleftrightarrow{\mathbf{G}}(\mathbf{r}, \omega) = \frac{e^{ikr}}{r} \bigg[& \left(1 + \frac{i}{kr} - \frac{1}{k^2 r^2}\right) \overleftrightarrow{\mathbf{I}} \\ & - \left(1 + \frac{3i}{kr} - \frac{3}{k^2 r^2}\right) \mathbf{n} \otimes \mathbf{n} \bigg], \end{aligned} \tag{5}$$

where $\mathbf{r}$ is the position vector, with $r = |\mathbf{r}|$ and $\mathbf{n} = \mathbf{r}/r$. Here $\overleftrightarrow{\mathbf{I}}$ and $k = \omega/c$ are the identity matrix and the free space wave number, respectively.

To obtain the plasmonic band structure, we consider an infinite periodic chain with zero incident field. By applying Bloch's theorem, the coupled dipole equations can be transformed into the following eigenvalue equation:

$$[\alpha^{-1}\overset{\leftrightarrow}{\mathbf{I}} - \overset{\leftrightarrow}{\mathbf{H}}]\mathbf{P} = \mathbf{0}, \tag{6}$$

where $\mathbf{P} = [p_\mathrm{A}, p_\mathrm{B}, p_\mathrm{C}, p_\mathrm{D}]^T$. The 4×4 effective Hamiltonian $\overset{\leftrightarrow}{\mathbf{H}}$ has

$$H_{\delta\eta} = \begin{cases} \dfrac{\omega^2}{c^2}\displaystyle\sum_{n\in Z} M(n\mathbf{d} + \mathbf{r}_\delta - \mathbf{r}_\eta, \omega)e^{ik_x nd} & \delta \neq \eta, \\ \dfrac{\omega^2}{c^2}\displaystyle\sum_{n\in Z, n\neq 0} M(n\mathbf{d}, \omega)e^{ik_x nd} & \delta = \eta, \end{cases} \tag{7}$$

where $\delta, \eta \in$ [A, B, C, D] and k_x is the Bloch momentum. The band structure can be obtained by sweeping k_x across the first Brillouin zone. The blue solid lines in Fig. 1(b) show the band structure for the specific parameters $(p, q) = (\pm 0.5, \pm 0.5)$. In these situations, the ENPs are exactly aligned in a line with staggered spacings in the x direction. Note that in this case particles C and D can be obtained by simply translating A and B by $d/2$ towards the $+x$ direction, respectively. And now the plasmonic chain can be considered to be analogous to a Su-Schrieffer-Heeger (SSH) model [48,50], and the band structure of the chain is equivalent to folding the Brillouin zone of the primitive unit cell containing two ENPs, as illustrated in Fig. 1(b). Consequently, linear crossing emerges between the first (third) and second (fourth) bands at the Brillouin zone boundary. Complete band structures are given in Appendix C. These results are corroborated by the FEM simulations presented in Fig. 1(c). It is important to note that the CDM band structure exhibits a pronounced divergence near the light line. This divergence arises because the lattice summation in Eq. (7) contains terms that diverge at the light line [50,58]. However, in our scenario, the diverging singularity does not influence the synthesized WPs, as it is situated far from the band structure crossings, as discussed later.

The band degeneracy at the Brillouin zone boundary is protected by translational symmetry within the unit cell, which appears only when $(p, q) = (\pm 0.5, \pm 0.5)$. Consequently, any deviation of (p, q) from the values of $(\pm 0.5, \pm 0.5)$ results in the lifting of this degeneracy and a band gap. This is a critical feature that guarantees the presence of WPs within the parameter space (p, q, k_x). Figures 2(a) and 2(b) illustrate the band dispersion in the p-q space when $k_x = \pi/d$. The ideal WPs appear at $(\pm 0.5, \pm 0.5)$, as expected. To verify the linear dispersion in all directions near the WPs, we have also calculated the band dispersion in the k_x-q space at a fixed p, as shown in Figs. 2(c) and 2(d). In addition, we have derived an effective Hamiltonian around the WP which possesses a standard type-I Weyl Hamiltonian form [32]. More details are given in Appendix D. The stability of the WPs is demonstrated by introducing weak perturbations to the transverse shifts of ENPs, as shown in Appendix E. The topological charge of the WPs is determined by the Berry curvature over a closed surface that encloses the WP [25,36,38]. Figure 2(e) depicts a spherical surface surrounding a WP in the 3D synthetic space. The topological charge of WPs can be deduced by tracking the evolution of the Berry phase from the north pole to the south pole of the sphere [25,36]. Note that here the Berry phase was calculated under the quasistatic approximation, a method widely used for characterizing the topology of plasmonic arrays [48,49,52–54]. Figure 2(f) presents the calculation results. It is observed that the topological charges of the WPs associated with the same bands at $(-0.5, -0.5)$ and $(0.5, 0.5)$ are opposite to those at $(-0.5, 0.5)$ and $(0.5, -0.5)$, with a net charge of zero in the synthetic space. This outcome is consistent with real 3D Weyl crystals [40–42], as the synthetic dimensions we consider are both periodic and self-consistent within the synthetic space.

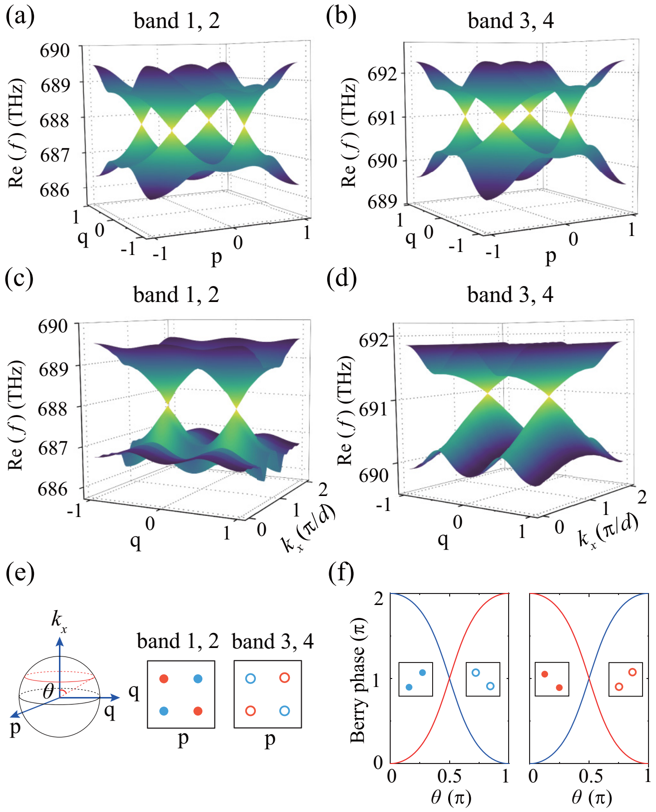

FIG. 2. (a) and (b) The dispersion of the chain in the p-q space with $k_x = \pi/d$. (c) and (d) The dispersion of the chain in the k_x-q space with $p = 0.5$. (e) Left: spherical surface centered at a WP in the 3D synthetic space. Middle and right: the positions of WPs in the p-q space appearing in (a) and (b), respectively. (f) Berry phases defined on the spherical surface with fixed θ, where blue and red lines represent Berry phases on the lower band and the upper band, respectively. The insets represent the corresponding WPs as marked in (e). The charges of WPs in the left and right panels are -1 and 1, respectively.

III. EDGE STATES AND BULK-EDGE CORRESPONDENCE IN THE SYNTHETIC 3D SYSTEM

To elucidate the Weyl topology physics of the synthetic 3D system, we now examine the eigenmodes of a finite plasmonic chain comprising 20 unit cells calculated using Eq. (3) under zero incident field. Figure 3(a) outlines the synthetic p-q space, in which the red (blue) circles denote the WPs that emerge between the first band and second band with

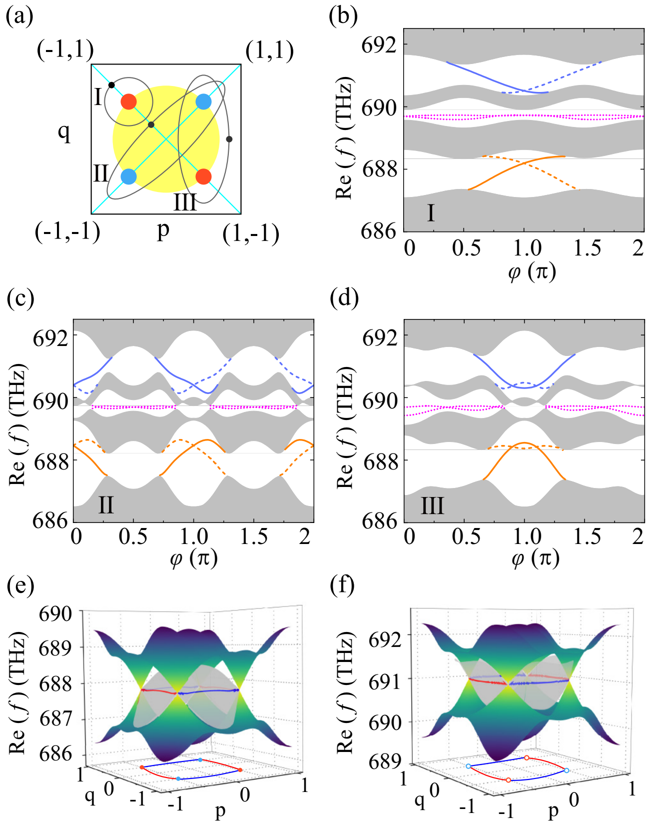

FIG. 3. (a) Synthetic *p*-*q* space; the red and blue circles represent the WPs. The closed loops labeled I, II, and III are the paths described by polar coordinate elliptic equations with angle parameter φ. The black dot marks the starting point of the path, e.g., $\varphi = 0$. The diagonal cyan lines are $p =$ q. The yellow shaded area and unshaded area correspond to the presence and absence of the edge states in the first gap, respectively. (b)–(d) Eigenmode spectrum evolution for a chain with 20 unit cells with p and q changing along the paths I, II, and III, respectively. The gray shaded areas are for bulk bands. The orange, pink, and blue solid (dashed) lines show the evolution of edge states with φ. (e) and (f) Edge states (transparent gray surfaces) appearing in the first and third gaps of the chain, respectively. The red and blue curves are the equifrequency contours connecting different WPs. The colored surfaces are band structures, which indicate the position of WPs and bulk gaps.

a topological charge of $+1$ (-1). The topological charge of these WPs endows the system with topological protected Weyl edge states, as ensured by the bulk-edge correspondence [32,34,35]. To identify the nontrivial Weyl topology of the chain, we can detect edge states along closed paths in the *p*-*q* space. We initially consider a path involving only one of the WPs, as indicated by path I in Fig. 3(a). In this instance, the net topological charge of the closed loop is $+1$, which dictates the number of edge states traversing the bulk band gap in accordance with the bulk-edge correspondence. Figure 3(b) displays the eigenspectrum of the finite chain with parameters p and q following path I. It clearly reveals a pair of gapless edge states bridging the first and second bulk bands, with solid and dashed orange lines representing edge states localized on the left and right of the finite chain, respectively. Notably, similar gapless edge states with inverted slopes are observed between the third and fourth bulk bands, as shown by the blue lines in Fig. 3(b). This phenomenon occurs because the WPs appearing between the first and second bands have charge opposite to those between the third and fourth bands, as illustrated in Figs. 2(c) and 2(d).

To further elucidate the bulk-edge correspondence in the synthetic 3D system, we now consider paths that encompass multiple WPs. Figure 3(c) presents the eigenspectrum with parameters p and q evolving along path II, which includes two WPs with a charge of -1, as shown in Fig. 3(a). The net charge of path II is -2, corresponding to two pairs of gapless edge states that connect the first and second bulk bands [see Fig. 3(c)]. In contrast, path III, shown in Fig. 3(a), contains two WPs with charges that cancel each other out, resulting in zero net charge. As a result, the edge states between the first and second bulk bands in this scenario do not traverse the bulk band gap, as observed in Fig. 3(d). Similar patterns of edge state behavior are also evident in the gap between the third and fourth bulk bands. Figures 3(e) and 3(f) show the edge states that appear in the first and third band gaps, respectively. The red and blue curves are the equifrequency contours connecting WPs with opposite charges, which represent the Fermi arcs in the synthetic space (p, q).

In addition to the bulk-edge correspondence, Fig. 3 actually provides further insights. We now concentrate on the edge states that appear in the first gap, as indicated by the orange lines in Figs. 3(b)–3(d). In Fig. 3(b), the two edge states intersect at $\varphi = \pi$ and gradually descend into the bulk bands as φ moves away from π. The transformation of the edge states into the bulk states is also observed in paths II and III, as illustrated by the orange lines in Figs. 3(c) and 3(d), respectively. Furthermore, the *p*-*q* space can be partitioned into two regions based on the existence of edge states in the first gap. As shown in Fig. 3(a), the yellow shaded and unshaded areas in the *p*-*q* space correspond to the presence and absence of the edge states in the first gap, respectively. It is evident that these two regions are centered around (0, 0) and (±1, ±1), respectively. It is also noteworthy that the intersection points of these paths with the lines $p = \pm q$ [the cyan lines in Fig. 3(a)] within the yellow shaded area correspond to the degenerate points of the edge states in the first gap.

To deeply understand the topological origin of the edge states in the synthetic 3D system, we have computed the Zak phase of the plasmonic chain. Despite the spatial symmetries of the chain being broken in most regions of *p*-*q* space, the inversion symmetry can be maintained when $p = q$ or $p = -q$. In these cases, the Zak phase can be quantized, serving as a topological invariant for the chain. The Zak phase is given by [54]

$$\gamma = \sum_{\text{occupied}} \int dk_x \mathbf{A}_n, \tag{8}$$

where the integral is taken over the first Brillouin zone. The Berry connection is defined as $\mathbf{A}_n = i \langle u_{k_x,n}| \nabla_{k_x} |u_{k_x,n}\rangle$, where n represents the band under the gap and u_{k_x} is the periodic part of the Bloch wave function [6,48]. The gray solid line in Fig. 4(a) shows the Zak phase of the first gap for $p = \pm q$. It is worth noting that the Zak phases are identical for both $p = q$ and $p = -q$, as Eq. (2) is an even function. The

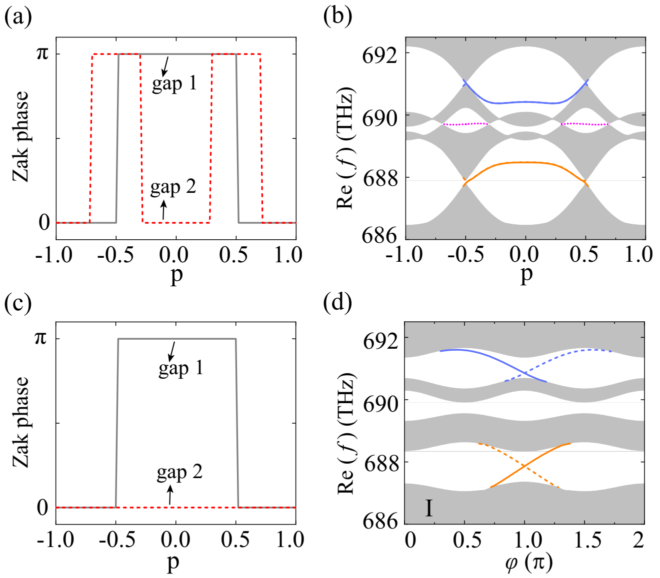

FIG. 4. (a) and (c) Zak phase of the first and second gaps when $p = q$ with $\Delta x = 3$ nm and $\Delta x = -3$ nm, respectively. (b) Eigenspectrum of the 20 unit-cell plasmonic chain when $p = q$ with $\Delta x = 3$ nm. The colored lines represent the doubly degenerate edge states. (d) Eigenspectrum of the 20 unit-cell plasmonic chain with p and q changing along path I with $\Delta x = -3$ nm.

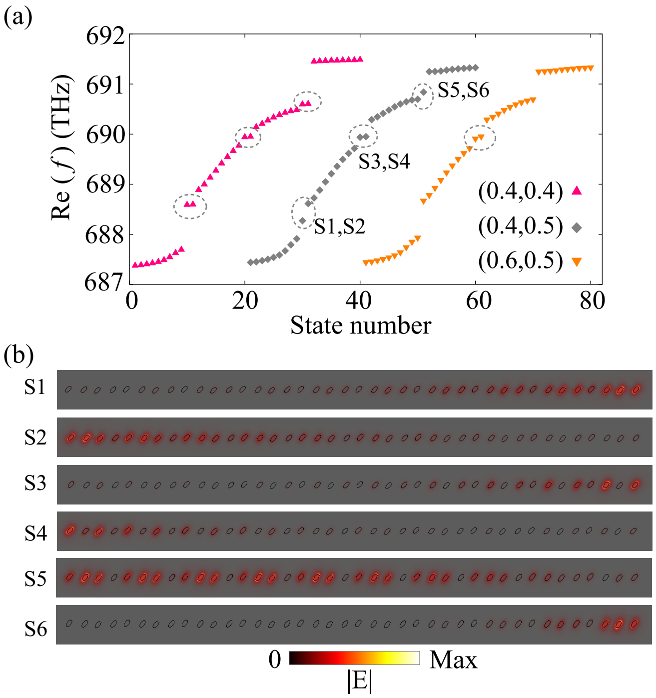

FIG. 5. FEM full-wave simulations. (a) Eigenmodes of a 10-unit-cell chain with different (p, q). (b) Electric field intensity distribution of the edge states labeled in (a).

Zak phase of the first gap is π (0) when $p \in (-0.5, 0.5)$ $[p \in (-1, -0.5) \cup (0.5, 1)]$, indicating that the first gap of the chain is in a topological nontrivial (trivial) phase. Figure 4(b) shows the eigenspectrum of a finite plasmonic chain with $p = q$. The edge states in the first gap are doubly degenerate due to the nontrivial Zak phase of the chain with the inversion symmetry. Topological phase transitions of the first gap occur at $(p, q) = (\pm 0.5, \pm 0.5)$, coinciding with the locations of the WPs in the synthetic 3D system. Notably, the degenerate points of the edge states observed in Figs. 3(b)–3(d) can be attributed to the quantized nontrivial Zak phase of the chain, while the absence of the edge states near $(p, q) = (\pm 1, \pm 1)$ is due to the trivial phase of the chain. These analyses are also applied to the edge states appearing in the third gap because the Zak phase of the third gap is consistent with the first gap according to our calculations. These findings reveal the intrinsic connection between the topology of the synthetic 3D WPs and the 1D plasmonic chain, providing a deeper understanding of the topological nature of the edge states in the system.

The edge states that appear in the second gap [indicated by the purple dotted lines in Figs. 3(b)–3(d)] exhibit distinct characteristics compared to the Weyl edge states. The red dashed line in Fig. 4(a) represents the Zak phases of the second gap when $p = \pm q$. It is observed that the nontrivial topological phase of the second gap is near $(p, q) = (\pm 0.5, \pm 0.5)$, where the chain is dimerized, akin to the conventional SSH model depicted in Fig. 1(a). The topological phase of the second gap can be manipulated by the competition between the intra- and intercoupling of the chain [50,58]. To distinguish the edge states appearing in the second gap and those in the first (third) gap, we consider the scenario where $p = \pm q$ and $\Delta x = -3$ nm. In this case, the second gap of the plasmonic chain is in a topological trivial phase when $(p, q) = (\pm 0.5, \pm 0.5)$ due to the interchange between the intra- and intercoupling. Figure 4(c) shows the Zak phases for this case, indicating that the second gap has transitioned to a trivial phase. However, the Zak phase of the first gap remains unchanged compared to the case of $\Delta x = 3$ nm. This is attributed to the synthetic WPs arising from the artificial band folding, which are not influenced by perturbations in Δx. Figure 4(d) shows the eigenmodes of a finite plasmonic chain with p and q varying along path I with $\Delta x = -3$ nm. As expected, no edge states are observed in the second gap, while the edge states and the bulk-edge correspondence around the WP persists in the first (third) gap.

To further verify the theoretical analysis based on CDM presented above, we conducted full-wave simulations using the FEM solver (COMSOL). Figure 5(a) shows the simulated eigenspectrum of a finite chain with various (p, q) parameters, where the edge states are encircled by the dashed ovals. We observe that the edge states at $(p, q) = (0.4, 0.4)$ exhibit degeneracy across the three bulk gaps. This is a consequence of the inversion symmetry protecting these states in the chain. However, this degeneracy is absent at $(p, q) = (0.4, 0.5)$ and $(p, q) = (0.6, 0.5)$, where the inversion symmetry is broken. Additionally, the absence of edge states in the first and third gaps for $(p, q) = (0.6, 0.5)$ is noted. These results are consistent with our CDM analysis. Figure 5(b) shows the electric field intensity distribution of the edge states marked in Fig. 5(a). States S3 and S4 are conventional SSH edge states, with fields concentrated at the B and D and A and C ENPs, respectively. In contrast, states S1, S2, S5, and S6 are edge

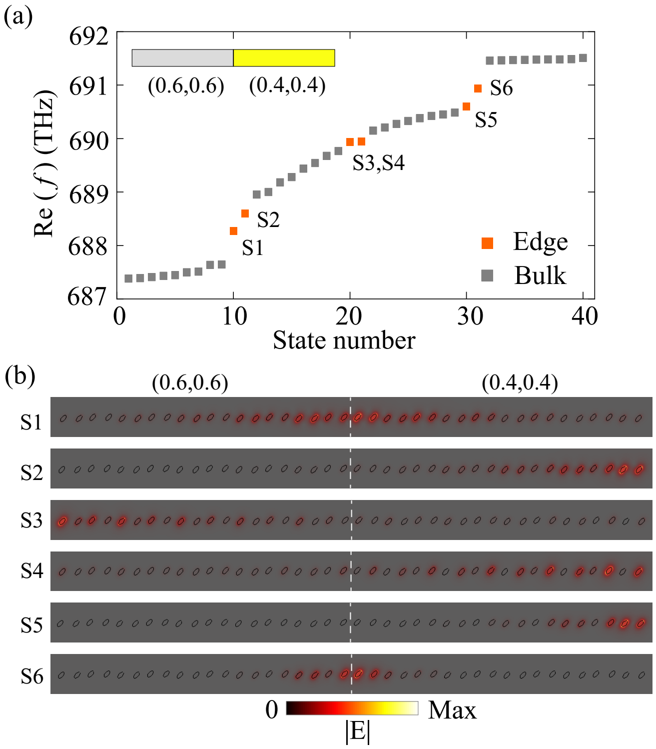

FIG. 6. FEM full-wave simulations of a chain consisting of five unit cells with $(p, q) = (0.6, 0.6)$ on the left and five unit cells with $(p, q) = (0.4, 0.4)$ on the right. (a) Eigenmodes of the chain. (b) Electric field intensity distribution of the edge states labeled in (a).

states linked to the synthetic WPs in the chain. The fields of S1 and S6 (S2 and S5) are located at the B, C, and D (A, B, C) ENPs, which is a distinct departure from the edge states observed in a typical SSH chain [50,58].

Finally, we examine the interface states between the chains with different (p, q). We consider a chain composed of two types of unit cells [left: $(p, q) = (0.6, 0.6)$; right: $(p, q) = (0.4, 0.4)$]. Interestingly, the interface states (S1 and S6 in Fig. 6) appear only in the first and third gaps. This is because the left and right unit cells are topologically opposite for both the first and third gaps, as shown in Fig. 4(a), even though they are close to the same WP, $(p, q) = (0.5, 0.5)$. On the contrary, the second gaps of both the left and right unit cells are topologically nontrivial, so the in-gap states appearing in the second gap are localized at the edges of the chain, as shown in Fig. 6, S3 and S4.

IV. CONCLUSION

In conclusion, we explored the Weyl physics in a chain of metallic ENPs. By introducing two additional positional parameters, we constructed a synthetic 3D space that allows for the realization of synthetic WPs within the 1D nanoscale system. As the parameters vary, the chain experiences transitions among phases with and without inversion symmetry. The topological properties of WPs ensure the existence of protected edge modes in the first and third bulk gaps, even when the chain's inversion symmetry is compromised. However, we demonstrated that degenerate edge modes are present in only the inversion-symmetric structures. Furthermore, by mapping the edge states along enclosed trajectories in the parameter space, we scrutinized the bulk-edge correspondence of the synthetic Weyl system, uncovering a striking resemblance to the characteristics of a genuine 3D Weyl system. The presence of edge modes in the chain was verified through comprehensive full-wave simulations, which revealed notable disparities when compared to the edge states in a typical SSH chain. Our results pave the way for manipulating topologically protected edge modes in low-dimensional plasmonic systems.

ACKNOWLEDGMENTS

This work was supported by the National Natural Science Foundation of China (Grant No. 62375064), the Shenzhen Science and Technology Program (Grants No. JCYJ20210324132416040 and No. KJZD20230923114803007), the Guangdong Provincial Nature Science Foundation (Grant No. 2022A1515011488), the National Key Research Development Program of China (Grant No. 2022YFB3603204), and the Guangdong Basic and Applied Basic Research Foundation (Grant No. 2023A1515110572).

APPENDIX A: THE OPTICAL RESPONSE OF AN INDIVIDUAL ENP

In this Appendix, we give a detailed description of the silver ENP used in the main text. The polarizability of the ENP has the following tensor form [54]:

$$\overleftrightarrow{\alpha}(\omega) = \begin{bmatrix} \alpha_a(\omega) & 0 & 0 \\ 0 & \alpha_b(\omega) & 0 \\ 0 & 0 & \alpha_c(\omega) \end{bmatrix}, \tag{A1}$$

where ω represents the angular frequency and α_l ($l \in [a, b, c]$) are the projections of the polarizability tensor in the directions of the axes of the ENP. The quasistatic polarizability is given by [59]

$$\alpha_l^s(\omega) = \frac{V}{4\pi} \frac{\epsilon(\omega) - \epsilon_b}{\epsilon_b + L_l[\epsilon(\omega) - \epsilon_b]}, \tag{A2}$$

where V is the ENP volume, $\epsilon_b = 1$ is the background dielectric constant, and L_l are static geometrical factors, with $L_a = 0.1736$ for the major axis and $L_{b(c)} = 0.4132$ for the minor axis [60]. Here $\epsilon(\omega)$ is the dielectric function of the ENP, which is given by the Drude model,

$$\epsilon(\omega) = \epsilon_\infty - \frac{\omega_p^2}{\omega^2 + i\omega/\tau}, \tag{A3}$$

with $\epsilon_\infty = 5$, $\omega_p = 1.36 \times 10^{16}$ rad/s, and $1/\tau = 5.88 \times 10^{13}$ rad/s [61]. i represents the imaginary unit.

Considering the radiative effects, we employ the modified long-wavelength approximation to describe α_l as [60]

$$\alpha_l(\omega) = \frac{\alpha_l^s(\omega)}{1 - \frac{Dk^2}{l}\alpha_l^s(\omega) - i\frac{2k^3}{3}\alpha_l^s(\omega)}, \tag{A4}$$

where $D, l, k = \omega/c_0$ and c_0 are the dynamic geometrical factor, axis half-length, wave number, and speed of light in free space, respectively.

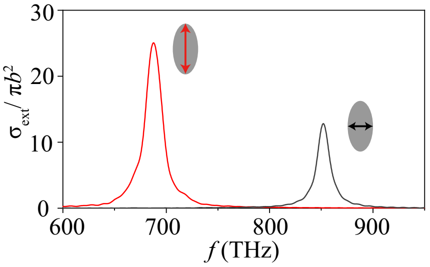

FIG. 7. Extinction cross sections of a silver ENP with major axis half-length $a = 10$ nm and minor axis half-length $b = c = 5$ nm, calculated by LUMERICAL FDTD. Red and black curves represent the extinction cross section of the ENP subjected to a field polarized parallel to and vertical to the major axis, respectively.

To analyze the optical response of the ENPs, we calculated the extinction cross section of a single ENP using LUMERICAL FDTD, as shown in Fig. 7. Red and black curves represent the response to a field polarized parallel and vertical to the major axis, respectively. It is seen that the ENP shows obvious resonance near $f = 690$ THz and $f = 850$ THz for the parallel and vertical polarized fields, respectively. In particular, the resonance is separated enough in the spectrum that one can use α_a as the polarizability of the ENP when the operating frequency is near $f = 690$ THz. Therefore, the polarizability of the ENP is set to $\alpha = \alpha_a$ in the main text.

APPENDIX B: COMPARISON OF DIFFERENT SCHEMES FOR ENP DISPLACEMENT

In the main text, the ENPs oscillate in the vertical direction. The vertical positions of the ENPs are used as the extra degrees of freedom for creating synthetic dimensions. Case I in Fig. 8(a) shows the relative position of two ENPs. The coupling between particles A and B calculated by Eq. (4) is shown by the red line in Fig. 7(b). Cases II–IV in Fig. 8(a) show other schemes for ENP displacement. The corresponding couplings between particles A and B are plotted in Fig. 8(b). Clearly, the relative variation range of the coupling in scheme I is greater than that of the other schemes. Therefore, the topological properties of an ENP chain in scheme I will change more significantly as the positional parameters evolve.

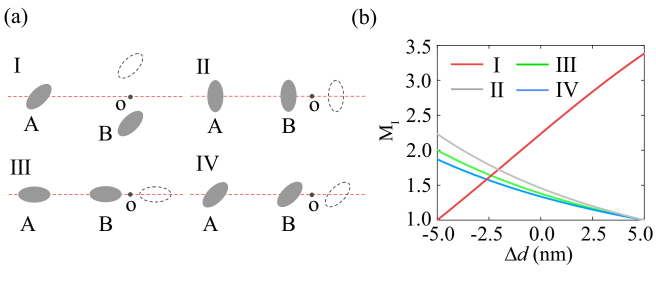

FIG. 8. (a) Different schemes for ENP displacement. A is fixed but B oscillates in the vertical (I) or horizontal (II–IV) direction around point o with 5 nm amplitude. The distance between the center of A and o is 40 nm. (b) The coupling between A and B under schemes I–IV, normalized by their minimum values. Δd is the offset of B relative to point o.

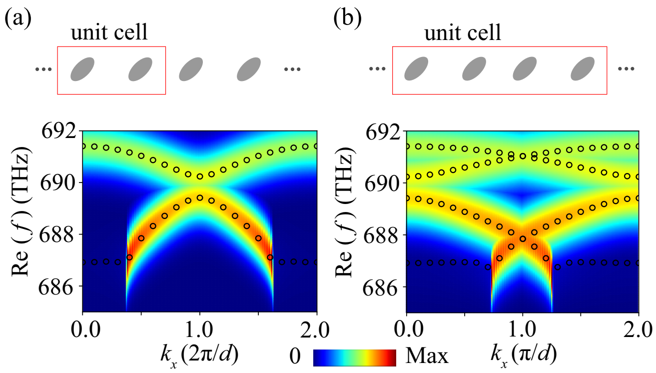

FIG. 9. Plasmonic band structures and spectrum of Im$(\alpha_{\rm eig})$ of the chain with $(p, q) = (\pm 0.5, \pm 0.5)$. (a) For the unit cell containing two ENPs. (b) For the unit cell containing four ENPs.

APPENDIX C: BAND STRUCTURES AND EFFECTIVE EIGEN-POLARIZABILITY

In this Appendix, we give the complete band structures of the plasmonic chain. As analyzed in Sec. II, the chain is analogous to a SSH model when $(p, q) = (\pm 0.5, \pm 0.5)$, which contains two ENPs within the primitive unit cell, as shown in the top panel in Fig. 9(a). The band structures can be obtained by solving

$$\det[\alpha^{-1}(\omega)\overleftrightarrow{\mathbf{I}} - \overleftrightarrow{\mathbf{H}}(k_x, \omega)] = 0, \tag{C1}$$

where $\overleftrightarrow{\mathbf{H}}$ is the corresponding effective Hamiltonian. To reduce computational complexity, we take the approximation $\omega = \omega_{sp}$ in the effective Hamiltonian, where $\omega_{sp} = \omega_p/\sqrt{\epsilon_\infty - 1 + L_a}$ is the surface plasmon frequency. The black circles in the bottom panel in Fig. 9(a) show the band structures of the primitive unit cell. Furthermore, we calculated the effective eigenpolarizability $\alpha_{\rm eig}$ of the chain, which is defined as $\alpha_{\rm eig} = \lambda^{-1}$, with λ being the eigenvalue of $[\alpha^{-1}(\omega)\overleftrightarrow{\mathbf{I}} - \overleftrightarrow{\mathbf{H}}(k_x, \omega)]$. In eigenresponse theory [62], the imaginary part of $\alpha_{\rm eig}$ exhibits a peak in the presence of a resonance. By sweeping both ω and k_x, the peaks of Im$(\alpha_{\rm eig})$ outline the band structures of the plasmonic chain. As shown in Fig. 9(a), the peaks of Im$(\alpha_{\rm eig})$ are consistent with the band structures.

The top panel in Fig. 9(b) shows the unit cell containing four ENPs. The corresponding band structures and spectrum of Im$(\alpha_{\rm eig})$ are plotted in the bottom panel in Fig. 9(b).

APPENDIX D: EFFECTIVE HAMILTONIAN NEAR WPs

In this Appendix, we derive the effective Hamilton around the WPs. Considering only the nearest-neighbor coupling, the Hamiltonian of the chain is

$$H = \begin{bmatrix} 0 & m_{\rm AB} & 0 & m_{\rm AD}e^{-ik_xd} \\ m_{\rm AB} & 0 & m_{\rm BC} & 0 \\ 0 & m_{\rm BC} & 0 & m_{\rm CD} \\ m_{\rm AD}e^{ik_xd} & 0 & m_{\rm CD} & 0 \end{bmatrix}, \tag{D1}$$

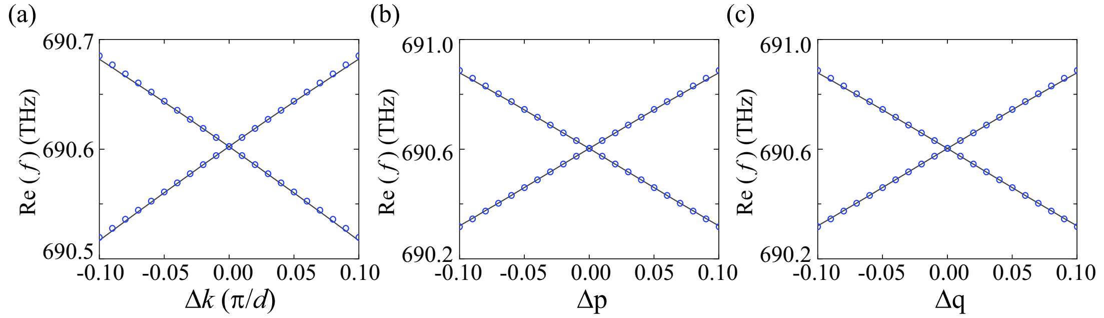

FIG. 10. The dispersion near the WP. The black lines are obtained with (D1), and the blue circles are the results from the effective Hamiltonian.

where $m_{\delta\eta}$ represents the coupling between two ENPs. Taking the quasistatic limit, we have

$$m_{\delta\eta} = \left[\left(-\frac{1}{r_{\delta\eta}^3}\overleftrightarrow{\mathbf{I}} + \frac{3}{r_{\delta\eta}^3}\mathbf{n}_{\delta\eta}\otimes\mathbf{n}_{\delta\eta}\right)\cdot\mathbf{I}_\delta\right]^T\cdot\mathbf{I}_\eta. \tag{D2}$$

We carry out a Taylor expansion of $m_{\delta\eta}$ at the WP, and by neglecting higher-order infinitesimal terms, we obtain

$$\begin{aligned} m_{\mathrm{AB}} &= a_1 + a_2(\Delta p - \Delta q),\\ m_{\mathrm{BC}} &= b_1 + b_2(\Delta p + \Delta q),\\ m_{\mathrm{CD}} &= a_1 + a_2(\Delta q - \Delta p),\\ m_{\mathrm{AD}} &= b_1 - b_2(\Delta p + \Delta q),\\ e^{\pm ik_xd} &= -1 \mp i\Delta k \end{aligned} \tag{D3}$$

where $\Delta p = p - 0.5$, $\Delta q = q - 0.5$, and $\Delta k = k_x - \pi/d$. The coefficients are $a_1 = \frac{1}{2x_{\mathrm{AB}}^3}$, $a_2 = \frac{3h\pi}{x_{\mathrm{AB}}^4}$, $b_1 = \frac{1}{2x_{\mathrm{BC}}^3}$, and $b_2 = \frac{3h\pi}{x_{\mathrm{BC}}^4}$.

H near the WPs can be block diagonalized into the following form:

$$U^{-1}HU = \begin{bmatrix} H^+ & 0\\ 0 & H^- \end{bmatrix}, \tag{D4}$$

where U is a unitary matrix composed of eigenvectors at the WP. H^+ (H^-) is the effective Hamiltonian around the upper (lower) band-crossing point and has the following elements:

$$\begin{aligned} H_{11}^+ &= \alpha_1 - (\alpha_2\Delta p - \alpha_3\Delta q),\\ H_{12}^+ &= \beta_1\Delta p + \beta_2\Delta q - i\beta_3\Delta k,\\ H_{21}^+ &= \beta_1\Delta p + \beta_2\Delta q + i\beta_3\Delta k,\\ H_{22}^+ &= \alpha_1 + (\alpha_2\Delta p - \alpha_3\Delta q), \end{aligned} \tag{D5}$$

where $\alpha_1 = u_1a_1 + u_2b_1$, $\alpha_2 = u_1a_2 + u_2b_2$, $\alpha_3 = u_1a_2 - u_2b_2$, $\beta_1 = u_1b_2 - u_2a_2$, $\beta_2 = u_1b_2 + u_2a_2$, and $\beta_3 = \frac{u_1b_1}{2}$, with $u_1 = 0.53725$ and $u_2 = 0.84343$. Then we can rewrite the effective Hamiltonian around $(\Delta p, \Delta q, \Delta k) = (0, 0, 0)$ as

$$H^+ = \alpha_1\sigma_0 + v_1\sigma_1 + v_2\sigma_2 + v_3\sigma_3, \tag{D6}$$

where $v_1 = \beta_1\Delta p + \beta_2\Delta q$, $v_2 = \beta_3\Delta k$, and $v_3 = \alpha_2\Delta p - \alpha_3\Delta q$. σ_0 and σ_i in (D6) are the identity matrix and Pauli matrices, respectively. The eigenvalues of H^+ are given by

$$E^+ = \alpha_1 \pm \sqrt{v_1^2 + v_2^2 + v_3^2}, \tag{D7}$$

which takes a cone-shaped band structure around the WP [33]. Similarly, the eigenvalues of H^- are

$$E^- = -\alpha_1 \pm \sqrt{v_1^2 + v_2^2 + v_3^2}. \tag{D8}$$

To verify the effective Hamiltonian, we plot the dispersion along three directions in Fig. 10. The results obtained with (D1) and the effective Hamiltonian agree very well near the WP.

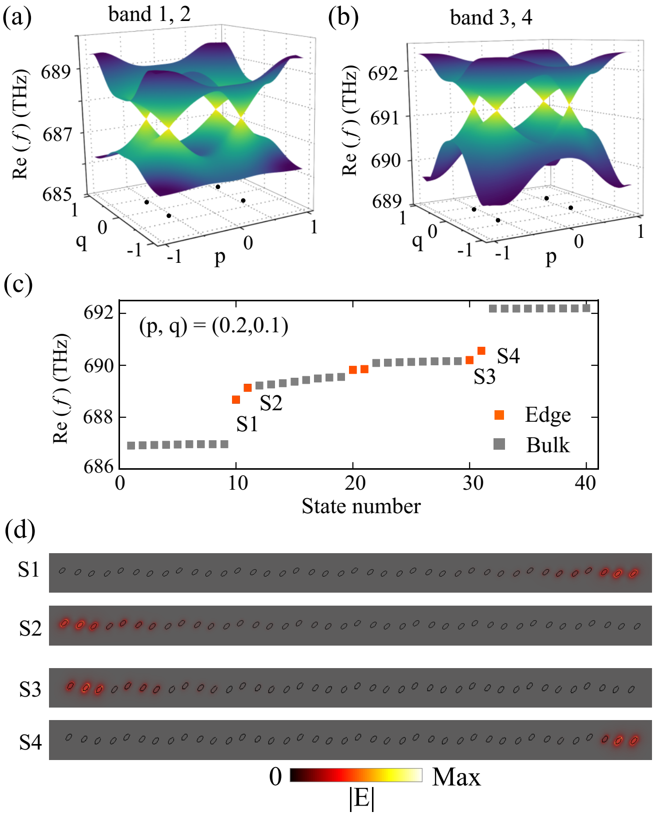

FIG. 11. (a) and (b) Band structure of the chain in the p-q space with $k_x = \pi/d$ under perturbations. The black dots in the p-q plane represent the projection positions of WPs. (c) Eigenmodes of a finite chain with $(p, q) = (0.2, 0.1)$. (d) Electric field intensity distribution of the edge states labeled in (c).

APPENDIX E: THE ROBUSTNESS OF THE WPs TO PERTURBATIONS

To demonstrate the stability of the WPs, we reset the vertical positions of the ENPs as

$$\begin{aligned} y_{\mathrm{A}} &= h\cos(p\pi) + \Delta y_{\mathrm{A}}, y_{\mathrm{C}} = -h\cos(p\pi) + \Delta y_{\mathrm{C}}, \\ y_{\mathrm{B}} &= h\cos(q\pi) + \Delta y_{\mathrm{B}}, y_{\mathrm{D}} = -h\cos(q\pi) + \Delta y_{\mathrm{D}}, \end{aligned} \tag{E1}$$

where Δy_η are the perturbation terms. More specifically, we set $\Delta y_{\mathrm{A}} = 3\,\mathrm{nm}$, $\Delta y_{\mathrm{B}} = -2.5\,\mathrm{nm}$, $\Delta y_{\mathrm{C}} = 2\,\mathrm{nm}$, and $\Delta y_{\mathrm{D}} = 3\,\mathrm{nm}$. Under these perturbations, the plasmonic chain still takes a cone-shaped band structure, but with the WPs moving from $(p, q) = (\pm 0.5, \pm 0.5)$ to $(p, q) = (\pm 0.52, \pm 0.32)$, as shown in Figs. 11(a) and 11(b). Figure 11(c) shows the eigenmodes of a finite chain with $(p, q) = (0.2, 0.1)$. The edge states, as shown in Fig. 11(d), still exist in the first and third bulk gaps, despite such perturbations.

[1] M. Z. Hasan and C. L. Kane, *Colloquium*: Topological insulators, Rev. Mod. Phys. **82**, 3045 (2010).

[2] X.-L. Qi and S.-C. Zhang, Topological insulators and superconductors, Rev. Mod. Phys. **83**, 1057 (2011).

[3] W. A. Benalcazar, B. A. Bernevig, and T. L. Hughes, Electric multipole moments, topological multipole moment pumping, and chiral hinge states in crystalline insulators, Phys. Rev. B **96**, 245115 (2017).

[4] Z. Song, Z. Fang, and C. Fang, $(d-2)$-dimensional edge states of rotation symmetry protected topological states, Phys. Rev. Lett. **119**, 246402 (2017).

[5] W. A. Benalcazar, T. Li, and T. L. Hughes, Quantization of fractional corner charge in C_n-symmetric higher-order topological crystalline insulators, Phys. Rev. B **99**, 245151 (2019).

[6] S. Vaidya, A. Ghorashi, T. Christensen, M. C. Rechtsman, and W. A. Benalcazar, Topological phases of photonic crystals under crystalline symmetries, Phys. Rev. B **108**, 085116 (2023).

[7] A. M. Marques and R. G. Dias, One-dimensional topological insulators with noncentered inversion symmetry axis, Phys. Rev. B **100**, 041104(R) (2019).

[8] J.-W. Rhim, J. Behrends, and J. H. Bardarson, Bulk-boundary correspondence from the intercellular Zak phase, Phys. Rev. B **95**, 035421 (2017).

[9] M. Xiao, Z. Q. Zhang, and C. T. Chan, Surface impedance and bulk band geometric phases in one-dimensional systems, Phys. Rev. X **4**, 021017 (2014).

[10] L. Lu, J. D. Joannopoulos, and M. Soljacic, Topological photonics, Nat. Photonics **8**, 821 (2014).

[11] J. Arkinstall, M. H. Teimourpour, L. Feng, R. El-Ganainy, and H. Schomerus, Topological tight-binding models from nontrivial square roots, Phys. Rev. B **95**, 165109 (2017).

[12] M. Kremer, I. Petrides, E. Meyer, M. Heinrich, O. Zilberberg, and A. Szameit, A square-root topological insulator with non-quantized indices realized with photonic Aharonov-Bohm cages, Nat. Commun. **11**, 907 (2020).

[13] A. M. Marques and R. G. Dias, 2^n-root weak, Chern, and higher-order topological insulators, and 2^n-root topological semimetals, Phys. Rev. B **104**, 165410 (2021).

[14] H. Wu, G. Wei, Z. Liu, and J.-J. Xiao, Square-root topological state of coupled plasmonic nanoparticles in a decorated Su-Schrieffer-Heeger lattice, Opt. Lett. **46**, 4256 (2021).

[15] L. Song, H. Yang, Y. Cao, and P. Yan, Square-root higher-order Weyl semimetals, Nat. Commun. **13**, 5601 (2022).

[16] D. Viedma, A. M. Marques, R. G. Dias, and V. Ahufinger, Topological n-root Su-Schrieffer-Heeger model in a non-Hermitian photonic ring system, Nanophotonics **13**, 51 (2024).

[17] V. M. Martinez Alvarez and M. D. Coutinho-Filho, Edge states in trimer lattices, Phys. Rev. A **99**, 013833 (2019).

[18] Y. V. Kartashov, A. A. Arkhipova, S. A. Zhuravitskii, N. N. Skryabin, I. V. Dyakonov, A. A. Kalinkin, S. P. Kulik, V. O. Kompanets, S. V. Chekalin, L. Torner, and V. N. Zadkov, Observation of edge solitons in topological trimer arrays, Phys. Rev. Lett. **128**, 093901 (2022).

[19] Z. Liu, G. Wei, and J.-J. Xiao, Geometric anisotropy induced higher-order topological insulators in nonsymmorphic photonic crystals, Phys. Rev. B **106**, 085415 (2022).

[20] Z. Guo, X. Wu, S. Ke, L. Dong, F. Deng, H. Jiang, and H. Chen, Rotation controlled topological edge states in a trimer chain composed of meta-atoms, New J. Phys. **24**, 063001 (2022).

[21] A. Celi, P. Massignan, J. Ruseckas, N. Goldman, I. B. Spielman, G. Juzeliunas, and M. Lewenstein, Synthetic gauge fields in synthetic dimensions, Phys. Rev. Lett. **112**, 043001 (2014).

[22] L. Yuan, Q. Lin, M. Xiao, and S. Fan, Synthetic dimension in photonics, Optica **5**, 1396 (2018).

[23] A. Dutt, M. Minkov, I. A. D. Williamson, and S. Fan, Higher-order topological insulators in synthetic dimensions, Light: Sci. Appl. **9**, 131 (2020).

[24] D. Yu, G. Li, L. Wang, D. Leykam, L. Yuan, and X. Chen, Moiré lattice in one-dimensional synthetic frequency dimension, Phys. Rev. Lett. **130**, 143801 (2023).

[25] Q. Wang, M. Xiao, H. Liu, S. Zhu, and C. T. Chan, Optical interface states protected by synthetic Weyl points, Phys. Rev. X **7**, 031032 (2017).

[26] X. Fan, C. Qiu, Y. Shen, H. He, M. Xiao, M. Ke, and Z. Liu, Probing Weyl physics with one-dimensional sonic crystals, Phys. Rev. Lett. **122**, 136802 (2019).

[27] Q. Lin, M. Xiao, L. Yuan, and S. Fan, Photonic Weyl point in a two-dimensional resonator lattice with a synthetic frequency dimension, Nat. Commun. **7**, 13731 (2016).

[28] D.-H.-M. Nguyen, C. Devescovi, D. X. Nguyen, H. S. Nguyen, and D. Bercioux, Fermi arc reconstruction in synthetic photonic lattice, Phys. Rev. Lett. **131**, 053602 (2023).

[29] L. He, Y. Li, B. Djafari-Rouhani, and Y. Jin, Hermitian and non-Hermitian Weyl physics in synthetic three-dimensional piezoelectric phononic beams, Phys. Rev. Res. **5**, 023020 (2023).

[30] Z. Liu, Q. Zhang, F. Qin, D. Zhang, X. Liu, and J. J. Xiao, Surface states ensured by a synthetic Weyl point in one-dimensional plasmonic dielectric crystals with broken inversion symmetry, Phys. Rev. B **99**, 085441 (2019).

[31] G. Wei, Z. Liu, H. Wu, and J. Xiao, Four dimensional second-order topological insulator based on a synthetic plasmonic metasurface, Opt. Lett. **46**, 4631 (2021).

[32] X. Wan, A. M. Turner, A. Vishwanath, and S. Y. Savrasov, Topological semimetal and Fermi-arc surface states in the electronic structure of pyrochlore iridates, Phys. Rev. B **83**, 205101 (2011).

[33] A. A. Soluyanov, D. Gresch, Z. Wang, Q. Wu, M. Troyer, X. Dai, and B. A. Bernevig, Type-II Weyl semimetals, Nature (London) **527**, 495 (2015).

[34] B. Yan and C. Felser, Topological materials: Weyl semimetals, Annu. Rev. Condens. Matter Phys. **8**, 337 (2017).

[35] N. P. Armitage, E. J. Mele, and A. Vishwanath, Weyl and Dirac semimetals in three-dimensional solids, Rev. Mod. Phys. **90**, 015001 (2018).

[36] M.-L. Chang, M. Xiao, W.-J. Chen, and C. T. Chan, Multiple Weyl points and the sign change of their topological charges in woodpile photonic crystals, Phys. Rev. B **95**, 125136 (2017).

[37] Z. Liu, G. Wei, H. Wu, and J.-J. Xiao, Möbius edge band and Weyl-like semimetal flat-band in topological photonic waveguide array by synthetic gauge flux, Nanophotonics **12**, 3481 (2023).

[38] Z. Fang, N. Nagaosa, K. Takahashi, A. Asamitsu, R. Mathieu, T. Ogasawara, H. Yamada, M. Kawasaki, Y. Tokura, and K. Terakura, The anomalous Hall effect and magnetic monopoles in momentum space, Science **302**, 92 (2003).

[39] J. Hu, S.-Y. Xu, N. Ni, and Z. Mao, Transport of topological semimetals, Annu. Rev. Mater. Res. **49**, 207 (2019).

[40] J. Noh, S. Huang, D. Leykam, Y. D. Chong, K. P. Chen, and M. C. Rechtsman, Experimental observation of optical Weyl points and Fermi arc-like surface states, Nat. Phys. **13**, 611 (2017).

[41] X. Shi and J. Yang, Spin-1 Weyl point and surface arc state in a chiral phononic crystal, Phys. Rev. B **101**, 214309 (2020).

[42] S. Vaidya, J. Noh, A. Cerjan, C. Jörg, G. von Freymann, and M. C. Rechtsman, Observation of a charge-2 photonic Weyl point in the infrared, Phys. Rev. Lett. **125**, 253902 (2020).

[43] M. Quinten, A. Leitner, J. R. Krenn, and F. R. Aussenegg, Electromagnetic energy transport via linear chains of silver nanoparticles, Opt. Lett. **23**, 1331 (1998).

[44] F. J. García De Abajo, *Colloquium*: Light scattering by particle and hole arrays, Rev. Mod. Phys. **79**, 1267 (2007).

[45] P. J. Compaijen, V. A. Malyshev, and J. Knoester, Time-dependent transport of a localized surface plasmon through a linear array of metal nanoparticles: Precursor and normal mode contributions, Phys. Rev. B **97**, 085428 (2018).

[46] C. Cherqui, M. R. Bourgeois, D. Wang, and G. C. Schatz, Plasmonic surface lattice resonances: Theory and computation, Acc. Chem. Res. **52**, 2548 (2019).

[47] M. S. Rider, A. Buendia, D. R. Abujetas, P. A. Huidobro, J. A. Sanchez-Gil, and V. Giannini, Advances and prospects in topological nanoparticle photonics, ACS Photonics **9**, 1483 (2022).

[48] C. W. Ling, M. Xiao, C. T. Chan, S. F. Yu, and K. H. Fung, Topological edge plasmon modes between diatomic chains of plasmonic nanoparticles, Opt. Express **23**, 2021 (2015).

[49] L. Wang, R.-Y. Zhang, M. Xiao, D. Han, C. T. Chan, and W. Wen, The existence of topological edge states in honeycomb plasmonic lattices, New J. Phys. **18**, 103029 (2016).

[50] S. R. Pocock, X. Xiao, P. A. Huidobro, and V. Giannini, Topological plasmonic chain with retardation and radiative effects, ACS Photonics **5**, 2271 (2018).

[51] M. Proctor, R. V. Craster, S. A. Maier, V. Giannini, and P. A. Huidobro, Exciting pseudospin-dependent edge states in plasmonic metasurfaces, ACS Photonics **6**, 2985 (2019).

[52] M. Proctor, M. Blanco de Paz, D. Bercioux, A. Garcia-Etxarri, and P. A. Huidobro, Higher-order topology in plasmonic kagome lattices, Appl. Phys. Lett. **118**, 091105 (2021).

[53] Q. Yan, E. Cao, Q. Sun, Y. Ao, X. Hu, X. Shi, Q. Gong, and H. Misawa, Near-field imaging and time-domain dynamics of photonic topological edge states in plasmonic nanochains, Nano Lett. **21**, 9270 (2021).

[54] A. Buendía, J. A. Sanchez-Gil, and V. Giannini, Exploiting oriented field projectors to open topological gaps in plasmonic nanoparticle arrays, ACS Photonics **10**, 464 (2023).

[55] H. Nielsen and M. Ninomiya, Absence of neutrinos on a lattice: (I). Proof by homotopy theory, Nucl. Phys. B **185**, 20 (1981).

[56] H. Nielsen and M. Ninomiya, Absence of neutrinos on a lattice: (II). Intuitive topological proof, Nucl. Phys. B **193**, 173 (1981).

[57] H. Nielsen and M. Ninomiya, A no-go theorem for regularizing chiral fermions, Phys. Lett. B **105**, 219 (1981).

[58] B. X. Wang and C. Y. Zhao, Topological phonon polaritons in one-dimensional non-Hermitian silicon carbide nanoparticle chains, Phys. Rev. B **98**, 165435 (2018).

[59] Y. Hadad and B. Z. Steinberg, Magnetized spiral chains of plasmonic ellipsoids for one-way optical waveguides, Phys. Rev. Lett. **105**, 233904 (2010).

[60] A. Moroz, Depolarization field of spheroidal particles, J. Opt. Soc. Am. B **26**, 517 (2009).

[61] H. U. Yang, J. D'Archangel, M. L. Sundheimer, E. Tucker, G. D. Boreman, and M. B. Raschke, Optical dielectric function of silver, Phys. Rev. B **91**, 235137 (2015).

[62] K. H. Fung and C. T. Chan, Plasmonic modes in periodic metal nanoparticle chains: A direct dynamic eigenmode analysis, Opt. Lett. **32**, 973 (2007).